
Understanding the diesel-like spray characteristics applying a flamelet-based combustion model and detailed large eddy simulations

Eduardo J Pérez-Sánchez¹, Jose M Garcia-Oliver² ,
Ricardo Novella²  and Jose M Pastor²

Abstract

This investigation analyses the structure of spray A from engine combustion network (ECN), which is representative of diesel-like sprays, by means of large eddy simulations and an unsteady flamelet progress variable combustion model. A very good agreement between modelled and experimental measurements is obtained for the inert spray that supports further analysis. A parametric variation in oxygen concentration is carried out in order to describe the structure of the flame and how it is modified when mixture reactivity is changed. The most relevant trends for the flame metrics, ignition delay and lift-off length are well-captured by the simulations corroborating the suitability of the model for this type of configuration. Results show that the morphology of the flame is strongly affected by the boundary conditions in terms of the reactive scalar spatial fields and $Z-T$ maps. The filtered instantaneous fields provided by the simulations allow investigation of the structure of the flame at the lift-off length, whose positioning shows low fluctuations, and how it is affected by turbulence. It is evidenced that small ignition kernels appear upstream and detached from the flame that eventually merge with its base in agreement with experimental observations, leading to state that auto-ignition plays a key role as one of the flame stabilization mechanisms of the flame.

Keywords

Combustion modelling, spray A, flamelet concept, auto-ignition, large eddy simulation turbulence model

Introduction

The restrictive normative that has been imposed during the last few years in the transport sector has prompted a deeper understanding of the complex phenomena that appear and interact in industrial combustion systems for their optimization in efficiency as well as in terms of pollutant emissions.

This task is far from being straightforward since the complete resolution of turbulent flows at high Reynolds numbers is nowadays unaffordable, forcing the introduction of stringent hypotheses. This situation becomes even worse when detailed chemistry is introduced due to the strong turbulence and chemistry interaction (TCI).¹ In addition, gathering experimental data is difficult in some ambient conditions as those found for diesel sprays complicating the advancement in the comprehension of this matter.

To shed light in this challenging topic, the engine combustion network (ECN) has suggested a set of

representative experiments to be conducted in special vessels, which tend to discard many uncertainties that would be found in a real engine. Such configurations have been extensively analysed by means of experiments and simulations by the scientific community. In addition, many advanced experimental techniques, with special emphasis on the optical ones, can be applied, providing very valuable information that can be used for modelling purposes also.

¹Barcelona Supercomputing Center-Centro Nacional de Supercomputación, Barcelona, Spain

²CMT-Motores Térmicos, Universitat Politècnica de València, Valencia, Spain

Corresponding author:

Ricardo Novella, CMT-Motores Térmicos, Universitat Politècnica de València, Edificio 6D, Camino de Vera s/n, 46022 Valencia, Spain.
Email: rinoro@mot.upv.es

Both constant-volume pre-burn (CVP) combustion vessels and constant-pressure flow (CPF) rigs have been used to characterize diesel-like sprays.^{3,4} A CPF rig is available at CMT-Motores Térmicos, the data of which are used throughout the article.^{5,6} The spray is characterized by means of the liquid and vapour penetrations as well as flame metrics like the ignition delay (ID) and lift-off length (LOL).

The wide measured data are used to investigate these experiments by means of computational fluid dynamics (CFD), which requires the use of several hypotheses both for turbulence and combustion. Obviously, there exist a very extensive variety of models which retain the physical and chemical aspects at different degree and that results in a wide range of computational cost.

Regarding turbulence both Reynolds-averaged Navier–Stokes (RANS) and large eddy simulations (LES) have been applied with an increasing use of the latter technique due to the availability of more computational resources. In RANS, fields are averaged over time or between realizations, and it is a quite extended approach in engineering applications due to its relative low computational cost. However, all the scales of the flow are modelled making the derivation of universal models almost impossible, since the largest vortexes are dependent on the boundary conditions and are highly anisotropic. Notwithstanding, excellent results have been obtained in the RANS framework and, more particularly, in combustion system simulations.^{7–9}

In LES, the instantaneous fields are decomposed into a filtered part (that we will denote with symbol \tilde{a}) and a fluctuating component related to the eddies not solved in the flow. The advantages of LES compared to RANS are that, on one hand, the most energetic spectrum of the flow is solved and, on the other hand, the vortexes not solved tend to be statistically isotropic and universal (not dependent on the boundary conditions) according to the Kolmogorov hypotheses,¹⁰ leading to more reliable turbulence models. Hence, the potential of LES lies on their high ability to reproduce the flow and provide accurate results.

Due to the higher computational cost related to LES simulations, it is quite extended to solve at most one single transport equation for the turbulence model, typically for the sub-grid kinetic turbulent energy k_{sgs} , which can be used in conjunction with models based on the Boussinesq hypothesis or, on the contrary, on scale similarity hypotheses to find the unresolved fluxes appearing in the momentum equations $\tau_{ij}^{sgs} = \overline{u_i u_j} - \tilde{u}_i \tilde{u}_j$ and the corresponding terms $\phi_i^{sgs} = \overline{\phi u_i} - \tilde{\phi} \tilde{u}_i$ in the equation of any general variable ϕ . Both can be applied together with the dynamic model in order to adjust the constants of the model based on the local behaviour of the flow. In this work, the potential provided by the LES simulations has been applied using the dynamic structure (DS) model,¹¹ which combines scale similarity hypotheses and the dynamic model, and has provided good results in the context of diesel spray simulations.^{12–14}

It is worth mentioning that, even if part of the inertial sub-range of the flow can be solved in LES simulations, no attempt of solving chemistry can be made with this approach, when considering that chemical reactions occur in the smallest scales of the flow and the application of a combustion model is still mandatory. In spite of that it is also true that the largest scales of the flow are better solved and the modelled component of the mixing variables has a lower weight in the predictions of the reactive scalars and their chemical source terms, implying an increase in the ability to reproduce combustion.^{15,16} Moreover, all these considerations make possible to directly extend many of the combustion models from RANS to LES.

Mixing variables are of paramount importance in non-premixed combustion, especially in flamelet-based models where the turbulent flame is described as an ensemble of strained laminar flames. Using this concept in conjunction with the intrinsic low-dimensional manifold (ILDm),¹⁷ the flamelet-generated manifold (FGM) and the flame prolongation of intrinsic low-dimensional manifold (FPI) were suggested.^{18,19} In LES, TCI is accounted for by means of filtered probability density functions (FPDFs) that are usually presumed and depend on some of the mixing variables solved in the flow. Such functions allow obtaining the turbulent reacting variable values from the laminar flame structure according to the main hypothesis of these models.

Flamelet models show a remarkable balance between accuracy and cost and have been successfully applied to many problems.^{7,18,20–23} However, in the case of diesel spray simulations, where boundary conditions span over large ranges and the use of complex chemical mechanisms is mandatory due to their transient nature and the difficulty in predicting pollutant emissions, some simplifications are required in order to reduce the computational cost while retaining the flame structure. With this aim, the approximated diffusion flamelet (ADF) model was suggested some years ago²⁴ and has proved to be accurate enough for its application to this kind of simulations.^{9,23,25–27}

This article presents an analysis of a reacting diesel-like spray by means of LES simulations in conjunction with a flamelet model. ECN spray A from ECN has been chosen since it has been targeted by many studies and, hence, it has become a sort of benchmark for this type of analysis. An oxygen parametric variation is performed to investigate how the model responds when the boundary conditions are changed. The main aim is to corroborate and harmonize the present simulation results with those found in the literature,^{28–33} as well as to show that the LES turbulence framework together with the flamelet-based combustion model and, more particularly, with the current implementation are suitable for modelling diesel-like flames, including the characteristics of the flame stabilization in the vicinity of the LOL.

Table 1. Definition of spray A parametric variations.

X_{O_2}	T_{amb} (K)	Z_{st}	Z_s
0.13	900	0.0403	0.326
0.15	750	0.0461	0.251
0.15	800	0.0461	0.278
0.15	850	0.0461	0.303
0.15	900	0.0461	0.326
0.21	900	0.0628	0.325

The article is structured as follows. First, the problem and modelling approach are described. Then, the validation of the model for inert conditions is given. This section is followed by the description of the reacting spray in terms of some of the flame metrics, which is linked with the description of the flame in physical space and $Z - T$ maps in order to understand the flame structure and how it is influenced by the oxygen concentration. The article ends with an analysis of the region of the base of the flame, that is, the zone at the LOL and the flame stabilization mechanism. Finally, the conclusion of the work closes the article.

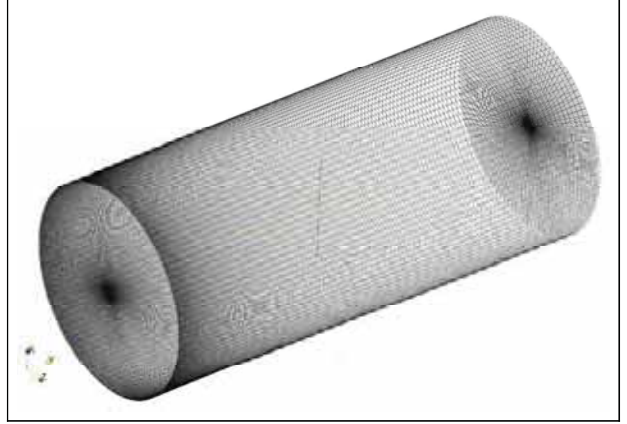
Problem description and modelling approach

As said earlier, the objective of this work is the analysis of the diesel spray structure and its dependence on the oxygen concentration by means of LES simulations applying a flamelet-based model. For this purpose, spray A from ECN, representative of modern diesel engines, has been chosen due to the relative wide experimental data available and the great effort carried out by the scientific community to investigate and deepen in its structure.

Although the work is focused on the effect of oxygen concentration, to show the ability of the model two parametric sweeps are considered in the ambient temperature and oxygen directions, whose boundary conditions are reproduced in Table 1. In all the cases, the ambient density is 22.8 kg m^{-3} , the fuel temperature 363 K, the injection pressure 150 MPa and a long injection rate ($\geq 4 \text{ ms}$) is imposed in order to describe the quasi-steady regime. Z_{st} from Table 1 refers to the stoichiometric mixture fraction, while Z_s is the saturation mixture fraction, that is the maximum mixture fraction for which fuel does not condensate and is calculated from a mixing-controlled approach.³⁴

The study by Desantes et al.³⁵ was focused on the ambient temperature sweep gathered in Table 1. Therefore, only some general results corresponding to these parametric variations are shown here in order to show the capabilities of the model, and the main analysis is focused on the oxygen sweep.

Spray A is a single nozzle spray with a nominal injector that measures $90 \mu\text{m}$ and has a nozzle code 210675² and discharge coefficient equal to 0.9.³⁶ As a

**Figure 1.** Three-dimensional view of the mesh and the domain.

diesel surrogate dodecane is used which is chemically described in the simulations using Narayanaswamy et al.'s³⁷ oxidation scheme, which comprises 255 species and 2289 reactions and has been widely extended in the literature.^{38,39}

CFD simulations are carried out using OpenFOAM toolbox⁴⁰ with an in-house developed code applying the volume finite method. Transport equations are solved by means of the PISO (Pressure-Implicit with Splitting of Operators) algorithm with second-order schemes to discretize the temporal, Laplacian and divergence terms.

The mesh is a cylinder with a height of 108 mm and a radius of 23.5 mm with open boundary conditions at all the faces except for the cylinder base, modelled as a wall, where the nozzle is positioned. The mesh is discretized in a total of 3.6 million cells that are distributed according to a cylindrical coordinate system with 108 cells in both radial and azimuthal directions and 292 cells in the axial coordinate. Expansion ratios of 1.015 and 1.01 were taken for radial and axial directions, respectively. In addition, in order to better solve the spray core an inner prism is defined with its axis coincident with that of the spray. Such a prism has a square base with side 1.688 mm and is composed of cells with square base and side of $62.5 \mu\text{m}$ according to the recommendations given in the literature for the use of Lagrangian models applied to liquid droplets.^{41,42} Different views of the mesh are given in Figures 1 and 2.

In order to solve the sub-grid stresses, the DS model,^{11,12,43} which transports k_{sgs} and uses scale similarity hypotheses, has been applied in the implementation given by Mompó.¹³ This model accounts for a term that describes the sub-grid interactions between the liquid droplets and the surrounding gas. Moreover, the liquid droplets are solved by means of the discrete droplet method (DDM), which comprises different models to describe the evolution of the droplets. The Reitz model⁴⁴ integrates the Kelvin–Helmholtz and Rayleigh–Taylor instabilities, while the Ranz–Marshall and O'Rourke models are applied to describe

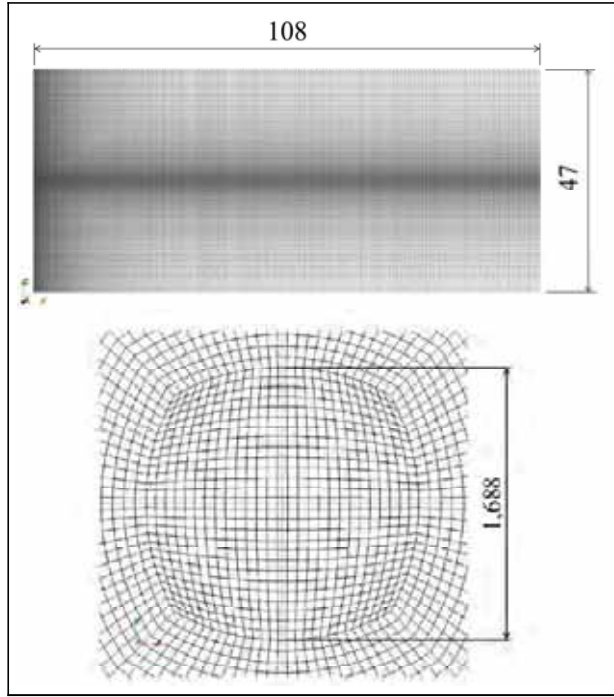


Figure 2. Different cuts of the mesh used for the calculations. Top figure shows a meridian plane. Bottom figure shows a perpendicular cut to the cylinder axis with a zoom at the inner prism. Dimensions are in mm.

evaporation and collision, respectively. Finally, droplets are injected according to a Rosin–Rammler distribution with a droplet diameter ranging from 10 μm to the nozzle diameter.

The combustion model is briefly explained here. The interested reader can find more details in the studies by Desantes et al.³⁵ and Pérez Sánchez.⁴⁵ As previously explained, the flamelet concept describes the turbulent flame as an ensemble of strained laminar flames where the gradients along the tangent directions are negligible compared to those found in the normal one. This leads to adopt a one-dimensional description for the laminar flames whose species transport equations can be written in the mixture fraction space as^{46,47}

$$\frac{\partial Y_k}{\partial t} = \frac{\chi}{2} \frac{\partial^2 Y_k}{\partial Z^2} + \dot{\omega}_k \quad k = 1, \dots, N \quad (1)$$

where Y_k and $\dot{\omega}_k$ are the mass fraction and chemical source terms for species k , respectively, Z is the mixture fraction and χ is the scalar dissipation rate. A profile is prescribed for χ , which can be split up in the strain rate a or χ at stoichiometry, χ_{st} , and mixture fraction contributions

$$\chi(a, Z) = \frac{a}{\pi} Z_s^2 \exp\left[-2(\text{erfc}^{-1}(2Z/Z_s))^2\right] = \chi_{st} \frac{F(Z)}{F(Z_{st})} \quad (2)$$

Equation (1) is solved for each of the species appearing in the oxidation scheme coupled with the chemical

ODE (ordinary differential equation) system. For large chemical schemes, this is expensive in terms of computational cost and the application of simplified models can reduce largely the computational time.

With this aim, the ADF model was devised by Michel et al.²⁴ The objective of this model, based on the flamelet equations, is to be able to manage very large chemical schemes, which are mandatory for diesel spray simulations, with a very reduced cost, and hence allowing the calculation of many sets of boundary conditions, while retaining the flame structure. The model relies on the ability to define a progress variable, on which all the variables depend on, that is representative of the combustion process. In this manner, the model only solves equation (1) for the progress variable Y_c which takes the form

$$\frac{\partial Y_c}{\partial t} = \frac{\chi(a, Z)}{2} \frac{\partial^2 Y_c}{\partial Z^2} + \dot{\omega}_c^{HR}(Z, Y_c) \quad (3)$$

where the chemical source terms for the progress variable $\dot{\omega}_c^{HR}(Z, Y_c)$ are computed from a set of homogeneous reactors (HRs), which are not computationally expensive, with the same initial and boundary conditions, than the laminar flames. Such chemical source terms and the reactive variables are tabulated as a function of the pair (Z, Y_c) and are retrieved by means of linear interpolations during the flamelet calculation, in the case of $\dot{\omega}_c^{HR}$, or during the post-processing, for the reactive scalars. In this work, the classical definition $Y_c = Y_{\text{CO}} + Y_{\text{CO}_2}$ ⁴⁸ has been taken.

First, the steady solutions are calculated with the application of the Newton–Raphson algorithm and then the transient solutions are obtained with an implicit algorithm where the derivatives in mixture fraction space are discretized with a second-order scheme and a first-order approximation is used for temporal derivatives with an adaptive time step. The implementation is carried out according to that given in the study by Payri et al.⁴⁹

Once the flamelets are solved, a laminar flame manifold in the form $\psi = \psi(Z, \chi_{st}, t)$ is obtained where ψ is any reactive scalar. In order to account for TCI, the manifold is integrated according to presumed FPDFs, which depend on variables solved in the turbulent flow

$$\begin{aligned} \tilde{\psi}\left(\tilde{Z}, \tilde{Z}_{sgs}^{\prime 2}, \tilde{\chi}_{st}, \tilde{t}\right) &= \int_0^{\infty} \int_0^{\infty} \int_0^{\infty} \psi(Z, \chi_{st}, t) \delta(t - \tilde{t}) \\ &\times P_Z\left(Z, \tilde{Z}, \tilde{Z}_{sgs}^{\prime 2}\right) \delta(\chi_{st} - \tilde{\chi}_{st}) dt dZ d\chi_{st} \end{aligned} \quad (4)$$

which becomes

$$\tilde{\psi}\left(\tilde{Z}, \tilde{Z}_{sgs}^{\prime 2}, \tilde{\chi}_{st}, \tilde{t}\right) = \int_0^{Z_s} \psi(Z, \tilde{\chi}_{st}, \tilde{t}) P_Z\left(Z, \tilde{Z}, \tilde{Z}_{sgs}^{\prime 2}\right) dZ \quad (5)$$

where \tilde{Z} is the filtered mixture fraction, while $\tilde{Z}_{sgs}^{\prime 2}$ is the sub-grid component of the mixture fraction variance. $\tilde{\chi}_{st}$ corresponds to the filtered scalar dissipation

rate at stoichiometry. The FPDF P_Z used for mixture fraction is a beta function.¹

In this way, a turbulent flame manifold in the form $\tilde{\psi} = \tilde{\psi}(\tilde{Z}, \tilde{Z}_{sgs}''^2, \tilde{\chi}_{st}, \tilde{Y}_c)$ (\tilde{t} is reparameterized with \tilde{Y}_c) is obtained. Applying equation (5) to χ , the following equation can be obtained

$$\tilde{\chi} = \tilde{\chi}_{st} J \left(\tilde{Z}, \tilde{Z}_{sgs}''^2 \right) \quad (6)$$

In this work, 32 values have been tabulated for \tilde{Z} , 17 for $\tilde{Z}_{sgs}''^2$, 35 for $\tilde{\chi}_{st}$, although these values may differ slightly depending on the boundary conditions, and 51 for \tilde{Y}_c with a parabolic distribution in order to retain accurately auto-ignition.

In the CFD calculation continuity, Navier–Stokes, energy and k_{sgs} equations are solved together with the transport equations for species (H, OH, CO, CO₂, H₂O, C₁₂H₂₆, CH₂O, C₂H₂, C₇H₁₄, H₂, O₂ and N₂).⁵⁰ The turbulent flame manifold is used to find the corresponding chemical source terms for the species transport equations according to

$$\tilde{\omega}_k = \frac{\tilde{Y}_k^{tab} \left(\tilde{Z}, \tilde{Z}_{sgs}''^2, \tilde{\chi}_{st}, \tilde{Y}_c(t + \delta\tau) \right) - \tilde{Y}_k}{\delta\tau} \quad (7)$$

where $\delta\tau$ is the CFD time step taken equal to 0.02 μ s. \tilde{Y}_k^{tab} corresponds to the value gathered in the turbulent flame manifold, while \tilde{Y}_k is the value at the cell at the current time step. The input variables to look for in the manifold and retrieve the value for \tilde{Y}_k^{tab} require to transport both \tilde{Z} and $\tilde{Z}_{sgs}''^2$, while $\tilde{\chi}_{st}$ is obtained from the pair $(\tilde{Z}, \tilde{Z}_{sgs}''^2)$ and $\tilde{\chi}$ by means of equation (6). To find the value of $\tilde{\chi}$, the solved component $2D|\nabla\tilde{Z}|^2$, with D the laminar mass diffusivity, and the sub-grid component are added. The last one is calculated with an algebraic model

$$\tilde{\chi}_{sgs} = C_\chi D_{sgs} \frac{\tilde{Z}_{sgs}''^2}{\Delta^2} \quad (8)$$

where C_χ is a constant to be calibrated.

Finally, the fourth input to enter in the manifold is $\tilde{Y}_c(t + \delta\tau)$, that is, the value of the progress variable if only combustion acted. As the chemical source term for variable Y_c , corresponding to the transient term $\partial Y_c / \partial t$ from equation (3) integrated according to equation (5), is saved in the manifold, $\tilde{Y}_c(t + \delta\tau)$ can be obtained as

$$\tilde{Y}_c(t + \delta\tau) = \tilde{Y}_c(t) + \frac{\partial \tilde{Y}_c}{\partial t} \left(\tilde{Z}, \tilde{Z}_{sgs}''^2, \tilde{\chi}_{st}, \tilde{Y}_c(t) \right) \delta\tau \quad (9)$$

The value of the progress variable $\tilde{Y}_c(t)$ at the cell and current time step is easily found from the vector of species mass fractions and the definition of the progress

variable. Once the species chemical source terms are obtained, their transport equations can be integrated closing the CFD calculation at the current time step.

Results and discussion

The analysis is divided into two sections. In the first section, a brief description of the flamelets for the oxygen sweep is given, and in the second section, first the model is validated in terms of the turbulent inert nominal case, and second the turbulent reactive spray and how it is influenced by the boundary conditions are described.

Flamelet results

In this section, a brief analysis of the flamelet behaviour in terms of their morphology and equation budget in Z space is given for the oxygen sweep. Figure 3 represents the inert and steady solutions together with different transient profiles for temperature. The curves correspond to cases $X_{O_2} = 0.13, 0.15$ and 0.21 , with $T_{amb} = 900$ K for low and high strain rates equal to 50 and 1000 s^{-1} , respectively. For each figure, the transient curves for the different cases have been chosen to represent similar states in the advancement of the flame. To better read the figure some markers have been added.

It is observed that the first stages of ignition (left column from Figure 3) are very similar for all the oxygen concentrations. It follows that during these first stages, the most reactive mixture fraction Z_{MR} ⁵¹ does not depend on the oxygen level. Ignition first occurs at lean mixtures but when temperature increased, it is rapidly displaced to rich mixtures. This is caused by the cool flames which are especially important in lean mixtures and freeze the advancement of such mixtures as can be observed by comparing left and centre columns.

However, once the first period of the flame ignition has been overtaken the development of the flame depends strongly on the oxygen concentration. In the case of $X_{O_2} = 0.21$, which is the most reactive case, chemistry is so intense and fast that by the time that the most developed mixtures have reached the steady solution only a very narrow range of mixtures have ignited reaching high temperatures, especially for low strain rates, since diffusion did not have time to transport quantities to other regions of the flow. In contrast with this, in the case with $X_{O_2} = 0.13$ high temperature region spreads over a very wide range when steady conditions are reached for the fastest mixtures. This behaviour is mitigated when the strain rate is increased since the intensity of diffusion gains specific weight compared to chemistry.

In addition, and as a consequence of the higher stoichiometric mixture fraction, Z_{MR} is noticeably richer for the high oxygen concentration compared to $X_{O_2} = 0.13$ when it reaches steady conditions, although it is observed, as noted previously, that Z_{MR} does not

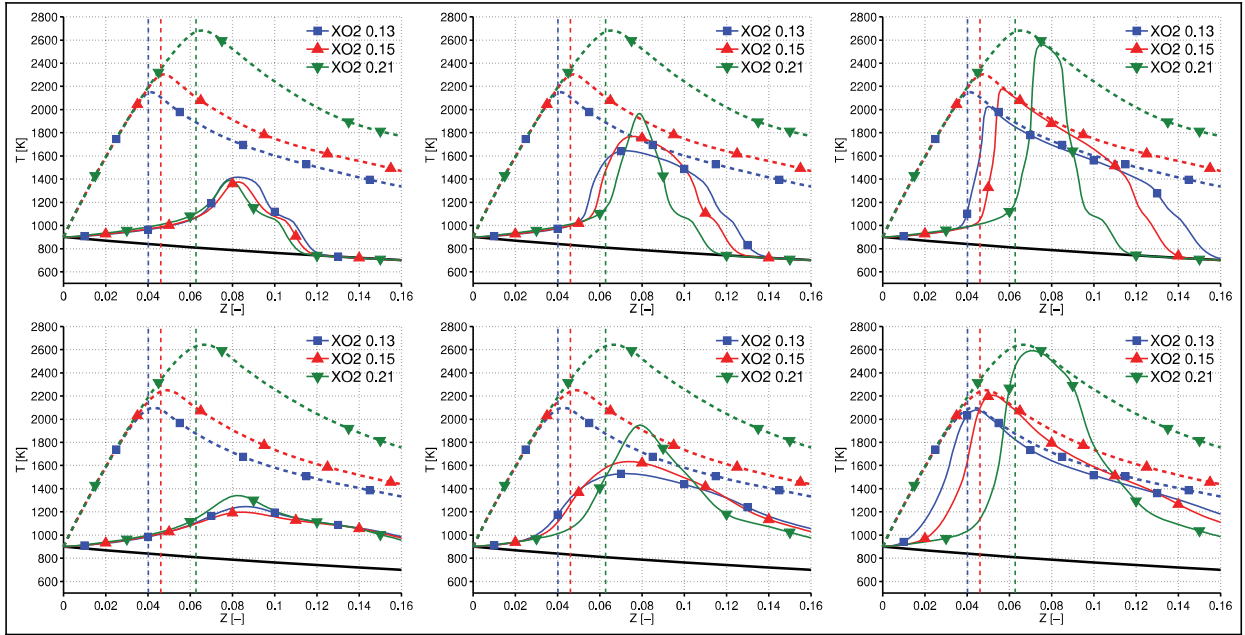


Figure 3. $Z - T$ flamelet curves for $X_{O_2} = 0.13, 0.15$ and 0.21 with $T_{amb} = 900$ K cases for strain rates $a = 50$ (top row) and 1000 (bottom row) s^{-1} . Each figure gathers a different transient state for each of the boundary conditions and previous strain rates. Figures include initial adiabatic mixing line (black) and for each case an intermediate profile (solid line) and the steady solution (dashed line). Vertical lines correspond to stoichiometric mixture fractions.

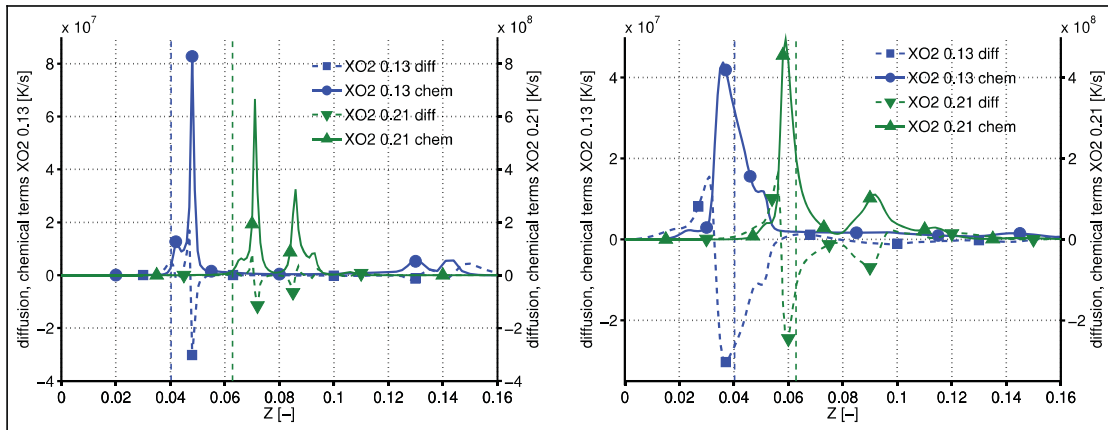


Figure 4. Budget for diffusion and chemical terms for temperature for $X_{O_2} = 0.13$ and 0.21 with $T_{amb} = 900$ K cases for strain rates $a = 50$ (left) and 1000 (right) s^{-1} . The budgets correspond to the transient profiles of the right column represented in Figure 3. Vertical lines correspond to stoichiometric mixture fractions.

depend on the oxygen concentration for intermediate temperatures. Finally, it is interesting to observe that the steady solutions are overlapped in the lean side independently of the oxygen concentration and such overlapping is detected as well for the transient profiles during the cool flame period of the lean mixtures (see left and centre columns in Figure 3).

In order to gain more insight about the relative specific weight of diffusion and chemical terms, the budget for these terms is represented in Figure 4 for the transient profiles of the right column shown in Figure 3 for the less and most reactive cases of the oxygen sweep,

that is, $X_{O_2} = 0.13$ and 0.21 . Again for reference some markers have been included.

According to the figures, two chemically active zones are detected corresponding to the range of mixtures that lie on both sides of the mixtures close to steady conditions with maximum slope. Due to rapid production of species and temperature in this region, a strong gradient is generated producing a negative flux to the surrounding mixtures. In this way, it can be observed that in the zones with high chemical activity, negative diffusion terms oppose to the chemical advancement of these mixtures. As expected, diffusion

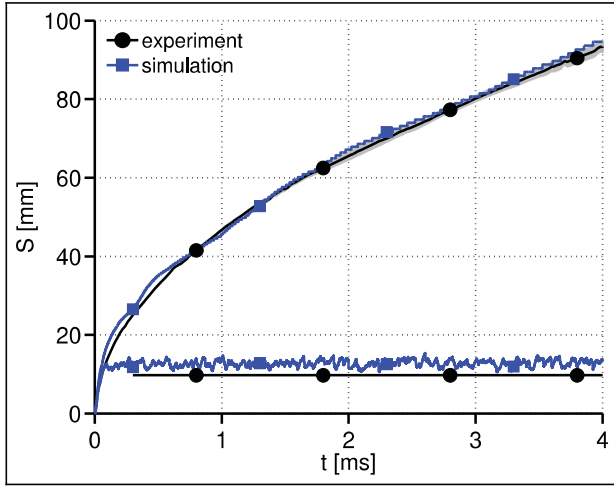


Figure 5. Vapour penetration and liquid length for experimental and simulated inert nominal conditions. For experiments, uncertainty of measurements is delimited with shadows.³⁵

tends to be as important as chemistry when the strain rate is increased.

As a summary, it is observed that when reactivity is decreased by means of oxygen concentration, the flame tends to flatten in mixture fraction space, that is, mixtures tend to advance in a more simultaneous way implying that the characteristics to ignite for different mixtures are more similar and, as a consequence, they are more prone to react when submitted to alike flow conditions. This conclusion will be used while analysing the behaviour at the base of the turbulent flame.

Validation of the turbulent spray model

Regarding the turbulent spray, first the model is validated under inert conditions in order to obtain a proper configuration of the turbulent and droplet model constants. As such configuration is the same as the one described in the study by Desantes et al.,³⁵ here only a shortened validation of the model is given.

Figure 5 shows the experimental and modelled vapour and liquid penetrations for the inert nominal case. The liquid length is defined as the distance to the nozzle where 95% of the injected liquid is found and the vapour penetration is given by the maximum distance from the nozzle outlet to the point on the axis where mixture fraction is 0.001.²

Despite the slight overestimation of the liquid length, the predicted value is acceptable and there exists an excellent agreement for the vapour penetration.

The averaged filtered fields for velocity and mixture fraction and its variance on the axis (or equivalently the mixture fraction root mean square Z_{rms}) are represented in Figure 6 again for the inert nominal case. For a clearer representation, some markers have been added. The measurements were obtained by means of Rayleigh imaging for the mixture fraction and particle image velocimetry (PIV) for the velocity.^{30,52–54} Axial distance is normalized by the equivalent diameter defined by $d_{eq} = d_0 \sqrt{\rho_f / \rho_a}$, where d_0 is the nozzle diameter and ρ_f, ρ_a are the fuel and air densities, respectively, since the simulations and the modelling have been performed with different nozzle diameters.

An excellent agreement is obtained for the variables shown in Figure 6 between simulations and experiments, confirming that the model reproduces the mixing and convective fields. Although not shown here, there exists a very good agreement in terms of radial profiles also. Moreover, it is observed that constant C_χ does not have a large influence on the predictions of mixture fraction variance since C_χ only influences the sub-grid component of the mixture fraction variance and there is a part of the variance which is solved in the flow from the fluctuations of the instantaneous mixture fraction field. Notwithstanding, even if C_χ has a weak influence on the sub-grid component of the mixture fraction variance, its choice could have some impact on $\tilde{\chi}$ and, consequently, on the ID and the LOL for the reacting conditions. To reach some insight on this aspect, Figure 7 represents $\tilde{\chi}$ (total scalar dissipation rate) profiles along the axis for the inert nominal

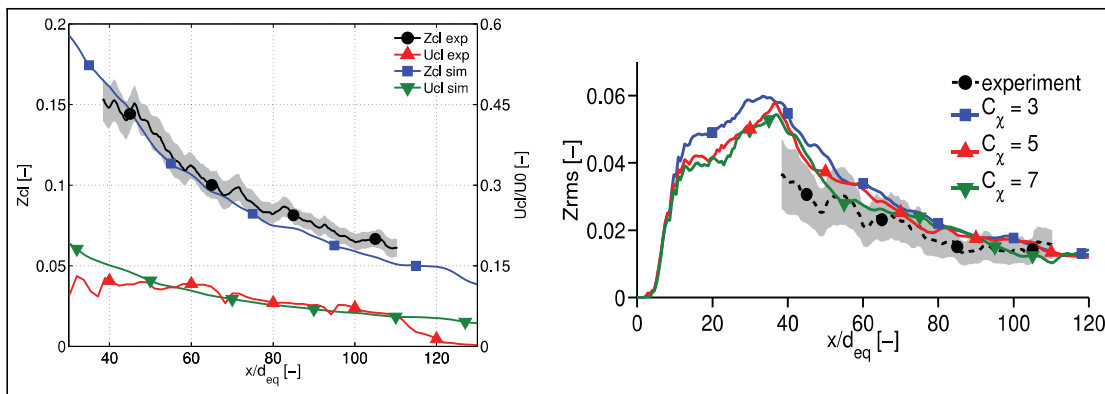


Figure 6. Spray validation for very advanced time instants. Left: averaged \tilde{Z} and normalized \tilde{U} on the centreline. Right: averaged Z_{rms} on the centreline for different C_χ values. Experimental uncertainties delimited with shadowed regions. Results for inert nominal condition.³⁵

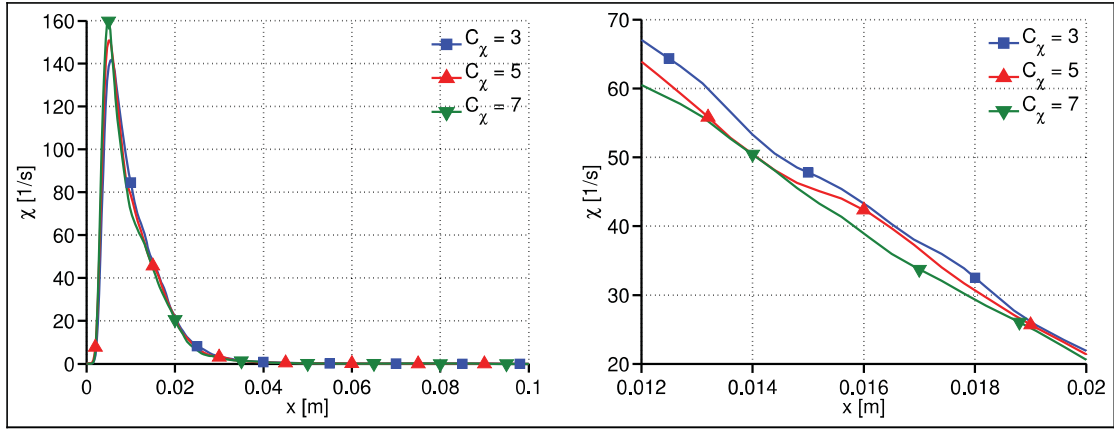


Figure 7. Left: temporally averaged $\tilde{\chi}$ on the centreline. Right: zoom of the temporally averaged $\tilde{\chi}$ profile along the axis in the vicinity of nominal lift-off length. Results for inert nominal condition.

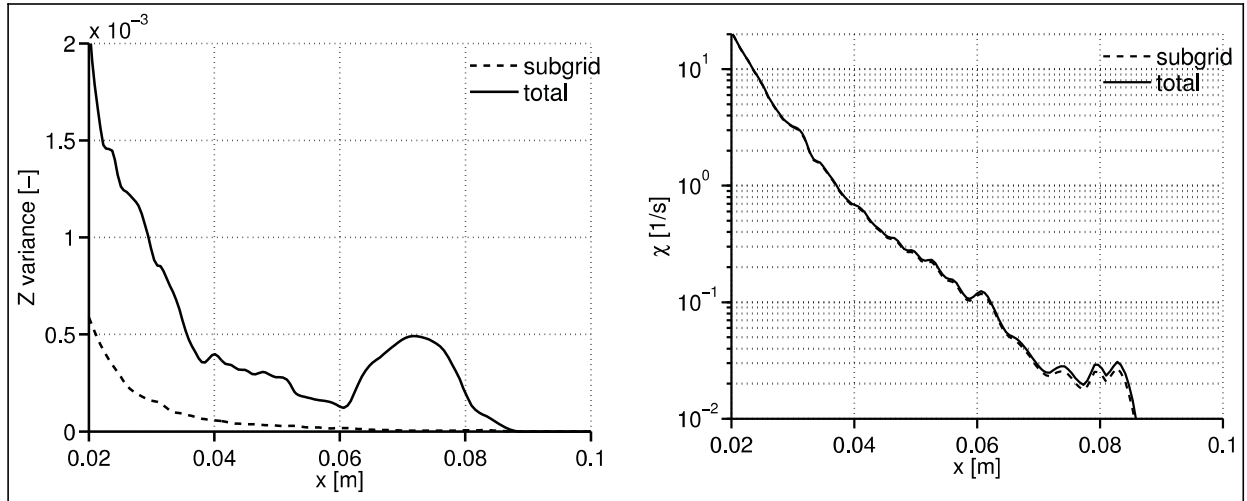


Figure 8. Total and sub-grid averaged $\widetilde{Z''^2}$ and $\tilde{\chi}$ variables on the axis. Results for inert nominal case.

case for different C_χ values. Profiles have been averaged over time.

It is seen that when C_χ is increased, the peak value found at approximately 5 mm is increased due to the enhancement of dissipation that makes the mixture fraction variances to decrease more rapidly. Subsequently, the $\tilde{\chi}$ values reached downstream are lower due to the lower mixture fraction variance values (Figure 6) as a consequence of the more intense dissipation that took place upstream. At first sight, it may seem that the influence of C_χ downstream 10 mm is marginal. In fact, the right plot of Figure 7 shows a zoom of $\tilde{\chi}$ axial profile in the vicinity of LOL (14.3 mm), evidencing that the effect of C_χ is locally quite sharp, since different values of $\tilde{\chi}$ are provided for the same axial position for each case. Nevertheless, as the slope of $\tilde{\chi}$ is very steep, such large differences are not so important when considering the vicinity to each point, for example, moving only 1 mm downstream along the $C_\chi = 3$ profile is enough to reach the same value as for $C_\chi = 7$.

As a consequence, the differences in the $\tilde{\chi}$ profile have a very reduced impact on spatial terms when C_χ is

changed. As the influence of C_χ is marginal on the mixture fraction variance and $\tilde{\chi}$ profiles, and it does not affect the instantaneous mixture fraction, the input data for entering in the flame manifold are not very influenced by the C_χ choice making the evolution of the progress variable and the rest of reactive scalars not very dependent on C_χ . Then, the influence on the flame metrics is expected to be much reduced. In this way, a value of $C_\chi = 5$ is finally chosen.

To deepen more in the mixing fields, Figure 8 represents the total and sub-grid profiles of the mixture fraction variance as well as of the scalar dissipation rate. The fields are temporally averaged. It is observed that a very important part of the mixture fraction variance is solved implying that the most energetic vortices are solved. However, the largest part of the scalar dissipation rate is modelled. This was expected since this variable measures the rate of dissipation of the mixture fraction variance and, consequently, according to the cascade energy hypothesis, this happens at the smallest scales of the flow which are not generally solved in an LES simulation. In addition, the minimum cell size of

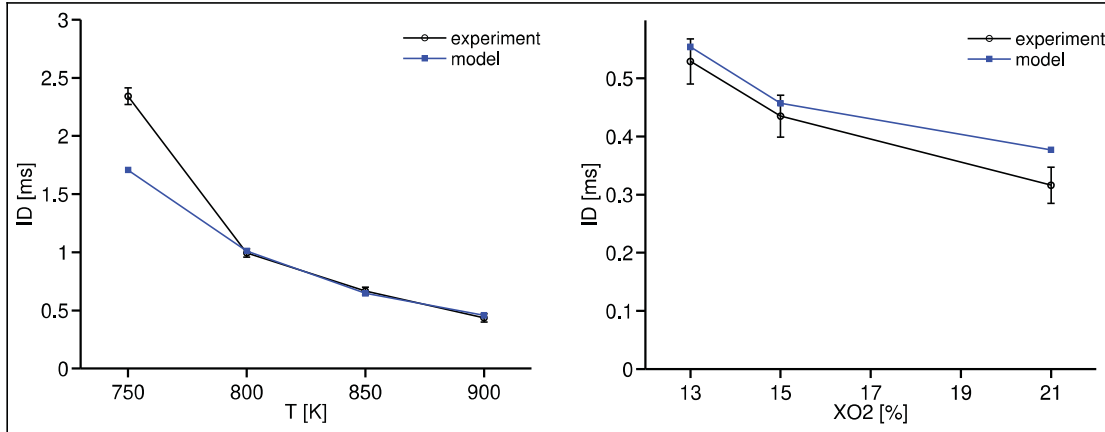


Figure 9. ID curves for the temperature (left)³⁵ and oxygen (right) parametric sweeps. Error bars delimit the standard deviation of the variable.

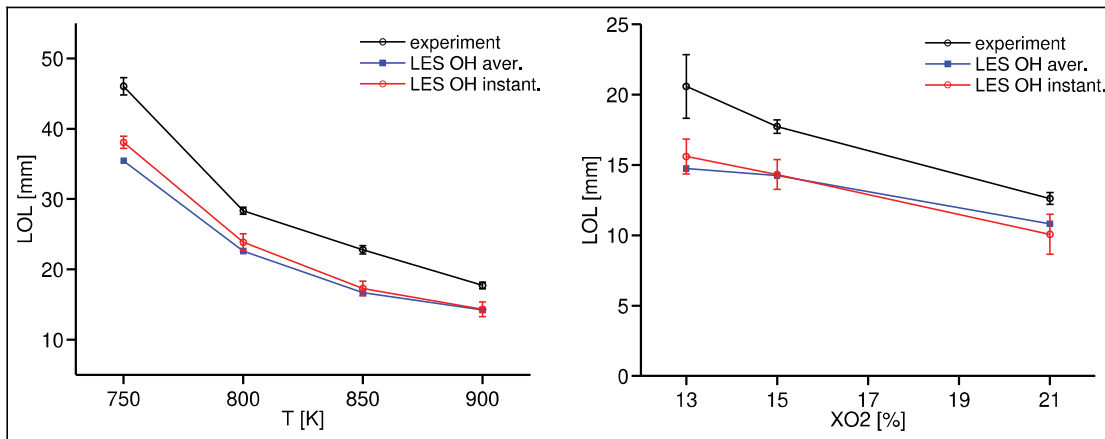


Figure 10. LOL curves for the temperature (left)³⁵ and oxygen (right) parametric sweeps. Error bars delimit the standard deviation of the variable.

$62.5 \mu\text{m}$ ^{41,42} that the DDM model imposes, in order to reduce to the maximum extent the volume of liquid in the cells close to the nozzle, prevents from refining the mesh and, hence, better solving the flow.

The validation shown in this section demonstrates that the simulations are able to reproduce the mixing fields and the spray structure and encourages further analysis, which is given in the following sections.

Description of the flame metrics

In this section, the predictions and trends of two of the most important flame metrics, namely ID and LOL, are described. Although the focus of the article is on the effect of ambient oxygen concentration, the temperature parametric variation is also included to show the predictive capability of the model. More details on this study can be found in the study by Desantes et al.³⁵

For modelling purposes and according to the ECN criterion,² ID is defined as the time spent from the start of injection until the maximum derivative of the maximum instantaneous Favre-filtered temperature field is

reached. The ID curves for both parametric sweeps are gathered in Figure 9. For LOL, two definitions based on hydroxide (OH) mass fraction have been considered. In both cases, LOL is defined as the minimum axial distance from the nozzle to the level curve corresponding to 14% of the maximum mass fraction of the OH field. In the first case, corresponding to the ECN criterion,² the averaged OH field is used (such field is obtained averaging the instantaneous fields temporally during 1 ms and azimuthally using 32 meridian planes). This case is denoted as ‘LES OH aver.’ In the second one, denoted as ‘LES OH instant.’, LOL is obtained averaging the distances measured applying such 14% to the instantaneous OH field. The advantage of the last definition is that a temporal profile of the LOL can be obtained and, hence, a fluctuation in its position can be estimated. The LOL curves for both parametric sweeps are gathered in Figure 10.

In general terms, the predictions for ID are excellent for both parametric sweeps with the only exception of the lowest temperature case for the ambient temperature sweep for which a premature ignition is observed

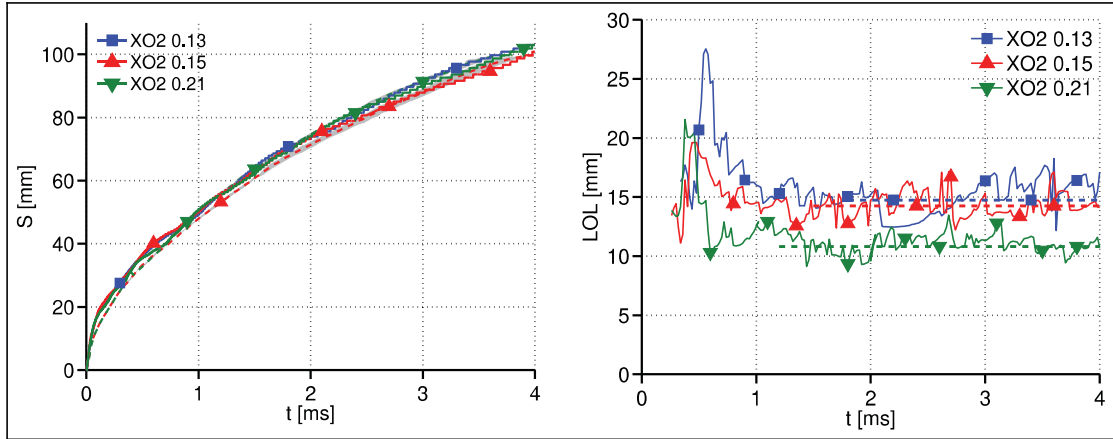


Figure 11. Left: reactive tip penetration for experimental (dashed line) and simulated (solid line) cases. For experiments, uncertainty of measurements is delimited with shadows. Right: LOL evolutions for the oxygen parametric sweep. Instantaneous signal represented with solid lines and ‘LES OH aver.’ included with dashed lines.

compared to experiments. Regarding LOL, although it is underestimated for all the conditions, the trends are well-reproduced since there exists a clear parallelism between modelled and experimental curves. In addition, both criteria provide very similar results demonstrating that the order of the operations (averaging OH field and measuring the distance and vice versa) does not have a strong impact on the final averaged result. It has been checked that parameter C_χ has a very weak influence on the ID, and it affects LOL in ± 1 mm, approximately. Considering both the mixture fraction variance profile (Figure 6) and the value of LOL, taking $C_\chi = 5$ provides a very good balance in terms of results.

The fact that the LOL is always underestimated may be a consequence, aside from some other minor aspects such as the chemical mechanism or the discrepancy between the experimental and modelling definitions for LOL, of the PDFs included in the integration, since for the scalar dissipation rate no PDF is accounted for and in its place a Dirac delta is imposed. The PDF for the scalar dissipation rate may have some relevance since $\tilde{\chi}$ is not expected to be solved in LES simulations, as was observed in Figure 8, due to the fact that it is related to the smallest scales of the flow and, as a consequence, the effect of its fluctuations should be described by a PDF. Although not considering a PDF for the scalar dissipation rate is a quite extended procedure,^{23,25,55} it may be insufficient for this particular problem and in this sense more research is needed.

As previously stated, ‘LES OH instant.’ definition allows estimation of the level of fluctuations of the LOL (this estimation does not consider sub-grid fluctuations but they are deemed to be small enough to not modify subsequent conclusions). According to the simulations, these fluctuations take similar values between 1 and 1.4 mm for all operating conditions. For the experiments, the standard deviation is found in the same order of magnitude although slightly smaller except for the case of $T_{amb} = 900$ K and $X_{O_2} = 0.13$.

These results show that the combustion model is able to reproduce the turbulent flame in terms of flame metrics and, hence, is suitable for these calculations.

A deeper insight of the behaviour of the LOL can be obtained representing the temporal evolution of the instantaneous LOL (‘LES OH instant.’) for the oxygen sweep variation. This is shown in Figure 11 where the ‘LES OH aver.’ values are also included. In addition, for reference the spray tip penetrations, defined in a similar way that the vapour penetration for inert case, are represented for the oxygen sweep in Figure 11. Only experimental results are available for the nominal and high oxygen concentration cases.⁴ Markers have been represented for reference.

An excellent agreement is observed in terms of reactive tip penetrations since the curves from the simulations fall pretty close to the measured ones. This means that the spray flow dynamics is adequately captured, which is governed by changes in air entrainment due to the inert to reacting transition. Small differences are observed among different oxygen concentration evolutions, both for experiments and simulated cases.

Regarding LOL, one interesting observation is that during spray auto-ignition the first ignition kernels always appear downstream of the stabilized LOL value followed by a rapid recession of LOL.^{56,57} This recession is slower and covers a larger distance for low reactive cases. Once LOL is stabilized it shows fluctuations of the order of ± 1 mm with no clear dependence of the level of such fluctuations on the boundary conditions. Moreover, time evolution shows that LOL suffers sudden jumps that seem almost discontinuities in its signal, for example, at 2 ms for $X_{O_2} = 0.13$ or 2.7 ms for $X_{O_2} = 0.15$. This is not caused by a rapid recession of LOL to upstream positions but to the apparition of detached and isolated burning pockets upstream of the base of the flame in agreement with experimental results³² and recent direct numerical simulations (DNS).⁵⁸ This will be described in more detail in later sections.

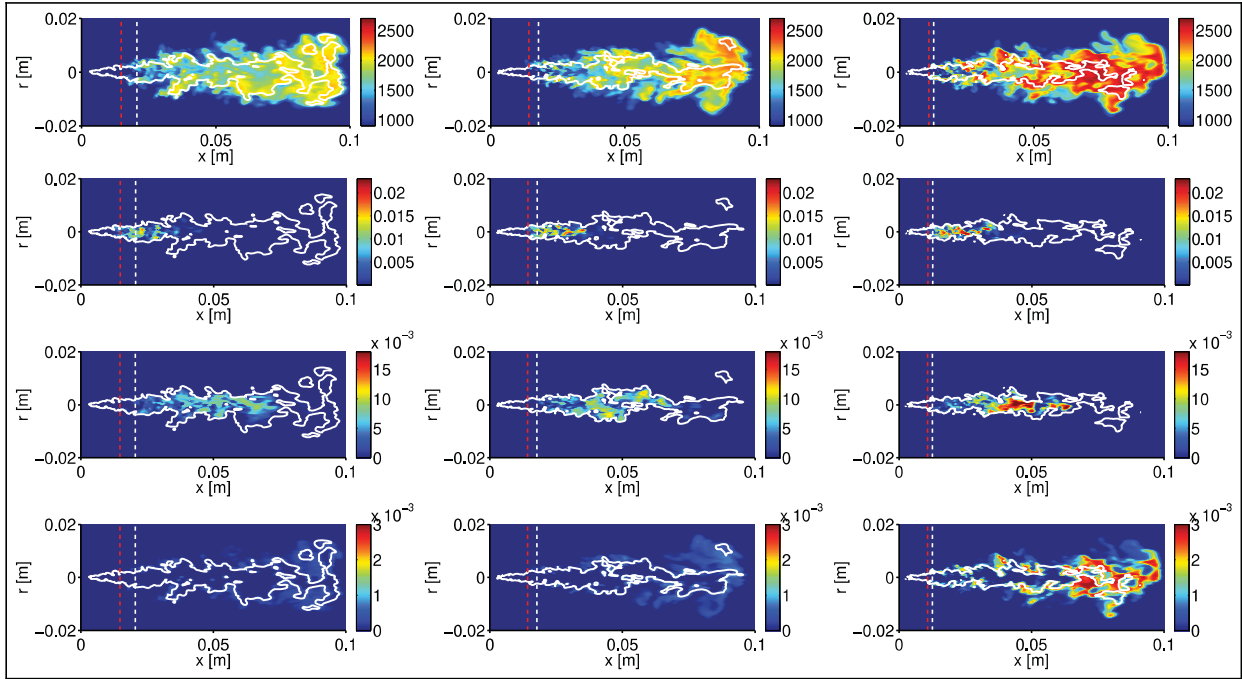


Figure 12. Instantaneous fields for \tilde{T} (first row), $\tilde{Y}_{\text{CH}_2\text{O}}$ (second row), $\tilde{Y}_{\text{C}_2\text{H}_2}$ (third row) and \tilde{Y}_{OH} (last row) for $X_{\text{O}_2} = 0.13$ (left), 0.15 (centre) and 0.21 (right) with $T_{\text{amb}} = 900$ K conditions. The level curve $Z = Z_{\text{st}}$ is included in white line. LOL values for experiment (white dashed) and simulation (red dashed) are also shown.

Instantaneous fields

This section describes the structure of the reacting spray by means of its representation in physical space and $Z - T$ maps for different reactive scalars at advanced instants once the spray has developed. Figure 12 shows the instantaneous fields for temperature and mass fraction for formaldehyde (CH_2O), which is a tracer of low temperature combustion, acetylene (C_2H_2) that is a soot precursor and, finally, hydroxide (OH) which is a tracer of high temperature combustion. Results for the oxygen parametric sweep are shown. All the fields correspond to an advanced instant once the base of the flame has stabilized.

The fields shown in Figure 12 reveal the structure of the reacting spray and how it is influenced by the boundary conditions. Chemical activity is negligible in the region between the nozzle and LOL, where the base of the flame is found, as there exist marginal traces of formaldehyde upstream of the LOL. At LOL location chemistry is triggered and, in a very reduced spatial path, temperature increases rapidly and high heat rates are released. At the base of the flame, a partially pre-mixed combustion region is found due to the dilution of the mixture. This region is composed of two lobes at each side of the axis (taking a meridian plane) since the region of the spray centreline is too rich to react at those residence times and, consequently, combustion is displaced to radial positions. However, when the reactivity is reduced by decreasing the oxygen concentration, the base of the flame is flattened, the residence times are higher and the whole region where

combustion develops tends to be more homogeneous, making the gradients less abrupt as shown in the case of $X_{\text{O}_2} = 0.13$. Moreover, it is observed that high temperature pockets emerge surrounding the stoichiometric level curve and alternate with colder mixture masses producing small vortexes due to the high shear stresses of this region.⁵⁹

The position where LOL is found is due to a balance between the chemical intensity and the flow dynamics that allows, by means of diffusion, combustion to happen. The rapid ignition at the distance of LOL shows that chemistry is very intense in this region. As was observed in Figure 11, chemical activity is intense enough to produce relatively small fluctuations of LOL distance, leading to a stable and vigorous anchored flame at such distance.

Moving downstream, the spray is surrounded by a reacting layer where reactions are completed and where a diffusion flame is established at the periphery of the spray.²⁸ In the inner region of the flame, acetylene is found at rich mixtures with higher temperatures than formaldehyde with a zone where both species coexist and overlap. Finally, and surrounding the stoichiometric level curve mainly on the lean side, the highest hydroxide concentrations are found.

Figure 12 shows clearly that increasing oxygen concentration also augments the maximum temperature and peak values of the species mass fractions found in the domain due to the enhanced reactivity. However, this increase in the peak value is not necessarily translated into an increase in the species total mass in the domain. An interesting case of this observation is that the total

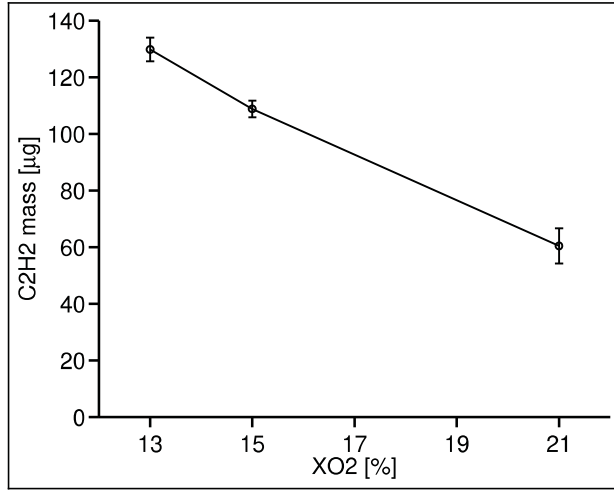


Figure 13. Acetylene total mass for the oxygen parametric sweep. Error bars delimit the standard deviation of the total mass.

mass of acetylene in the domain, which is important since it is a soot precursor, decreases when augmenting the oxygen concentration in agreement with previous RANS simulations carried out with this model.⁴⁵ This is shown in Figure 13 where the total mass found in the domain for acetylene is represented for the oxygen parametric sweep. The error bars indicate the standard deviation of the total mass and only consider the solved part of the field (the sub-grid component is not included). However, the high percentage of mixture fraction variance that is solved in the computation (see Figure 8) suggests that a very important part of the species mass fraction fluctuations are solved too, making representative the estimation of the fluctuations shown in Figure 13.

The cause of the reduction in the acetylene mass when the oxygen concentration is increased in spite of the augmentation of the peak values is found in the fact that increasing XO_2 provokes that combustion, which is mainly enclosed by the stoichiometric level curve, develops at closer positions to the spray axis since the stoichiometric mixture fraction is higher. Since in

statistical terms the spray shows cylindrical symmetry, the same mass fraction values produce smaller mass contributions if they are found nearer the centreline.

The whole picture of the flame structure given here agrees with classical works²⁸ and recent experimental findings.³⁰

In order to gain more insight, previous species are represented in $Z - T$ maps, shown in Figure 14, for the oxygen parametric sweep. For better visualization, only points with the species mass fraction higher than 0.25 of the maximum value are included. Moreover, the initial adiabatic mixing line and the upper contour of the map are shown.

The maps clearly reveal where the different species are positioned, namely, formaldehyde at rich mixtures and intermediate temperatures, acetylene at slightly leaner mixtures and temperatures close to the equilibrium for those mixtures and, finally, hydroxide at very high temperatures in the vicinity of the stoichiometric mixture fraction. Moreover, the reduction in LOL when the reactivity of the mixture is increased is translated into an enlargement of the reactive mixtures.

As a final observation, as was previously mentioned, it is noted that there exists a remarkable increase in the maximum temperature reached in the domain when the oxygen concentration is augmented.

Analysis of the flame at the LOL

This section is devoted to the analysis of how combustion develops at the base of the flame and it is aimed at gaining some more insight about the flame stabilization mechanism. First in order to evaluate the importance of extinction phenomena, the ratio between the stoichiometric scalar dissipation rate at LOL $\tilde{\chi}_{st}^{LOL}$ and the maximum stoichiometric scalar dissipation rate in the auto-ignition range calculated with the laminar flames $\chi_{st,flam}^{max}$, that is, the maximum χ_{st} for which the flame can evolve from inert to high temperatures close to equilibrium, is represented for the oxygen parametric variation in Figure 15. $\tilde{\chi}_{st}^{LOL}$ is considered for both the instantaneous LOL signal for the instantaneous $\tilde{\chi}_{st}$ field and for the position given by ‘LES OH aver.’ for

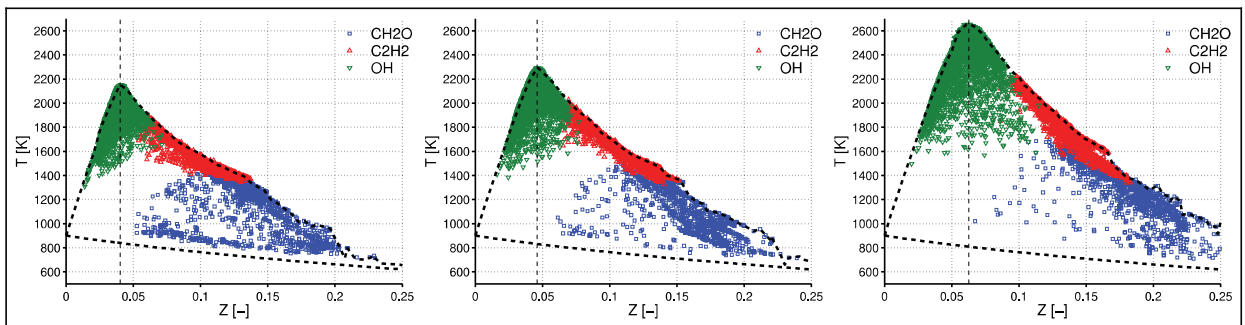


Figure 14. $Z - T$ maps for $XO_2 = 0.13$ (left), 0.15 (centre) and 0.21 (right) at $T_{amb} = 900$ K. Fields \tilde{Y}_{CH_2O} , \tilde{Y}_{OH} and $\tilde{Y}_{C_2H_2}$ are included. The adiabatic initial mixing and upper contour of the map are represented with black dashed lines. The stoichiometric value is shown with a vertical line.

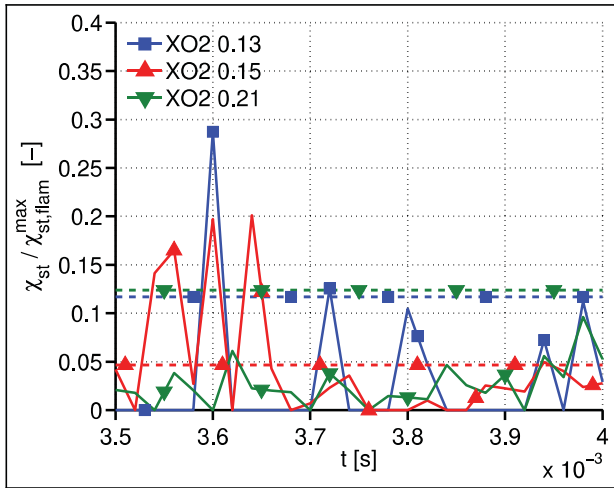


Figure 15. $\tilde{\chi}_{st}^{LOL} / \chi_{st,flam}^{max}$ ratio for the oxygen parametric sweep. Continuous line represents the profile computed from the instantaneous LOL position, while dashed line corresponds to the LOL distance found from ‘LES OH aver’.

the averaged $\tilde{\chi}_{st}$ field. Again some markers are depicted for reference.

From the figures, it is observed that the values reached at the LOL position are always low compared to the extinction limit (< 0.3) for all the boundary conditions. This means that extinction phenomena only may occur sporadically at the base of the flame and, in general, the base of the flame develops at low scalar dissipation rates⁵¹ discarding extinction phenomena as a possible stabilization mechanism for diesel flames.⁶⁰

Figure 16 shows a time evolution of the instantaneous temperature field for the oxygen parametric sweep in the region of the LOL for the modelled results. The figures include the instantaneous LOL value and the stoichiometric mixture fraction level curve. In addition, level curves for threshold values of ambient temperature plus 500 K are depicted for reference.

The first observation is that chemistry is very intense at LOL since a thin interface, which separates the unburned mixture from the partially burned products,

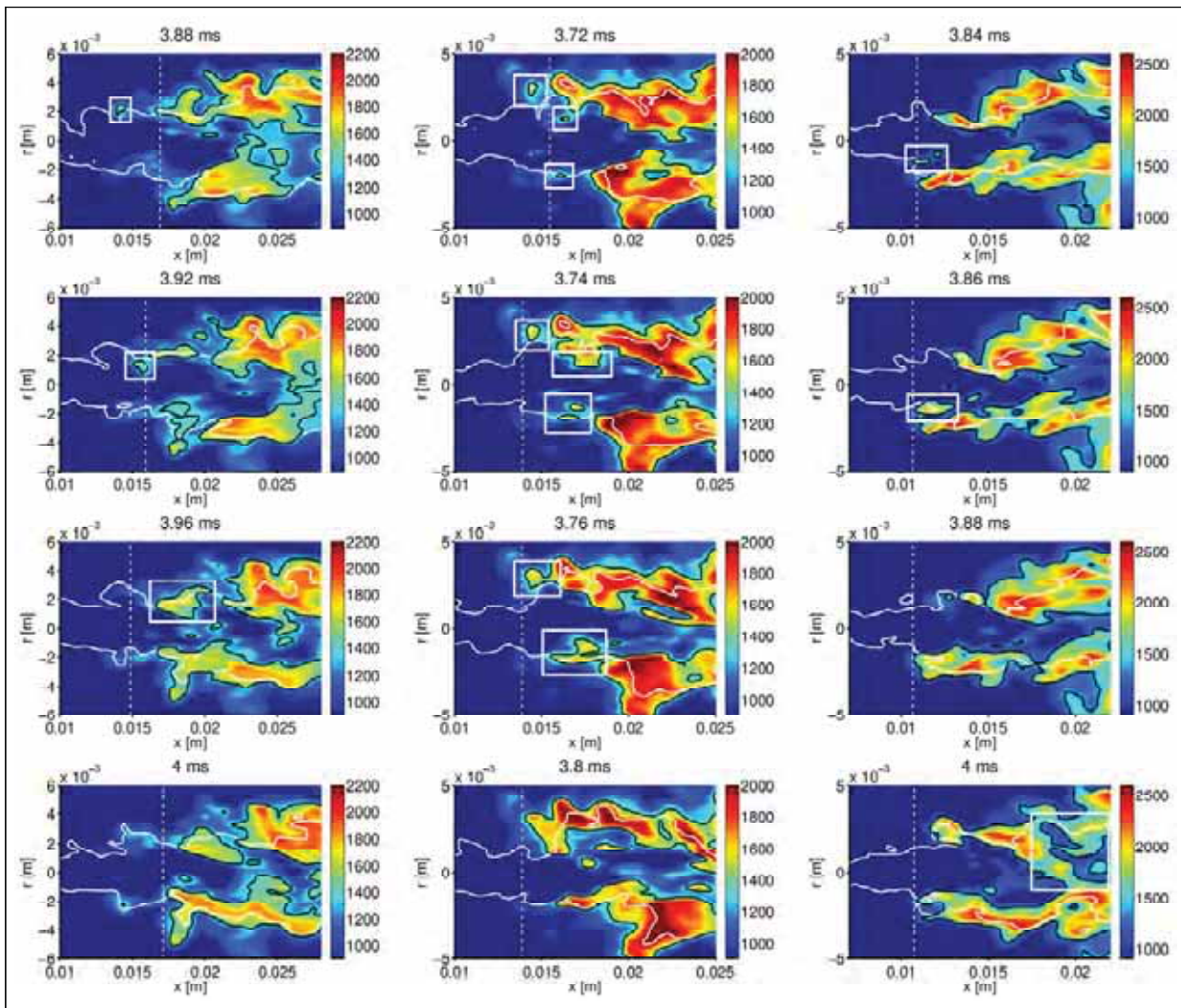


Figure 16. Instantaneous temperature fields for $X_{O_2} = 0.13$ (left), 0.15 (centre) and 0.21 (right) with $T_{amb} = 900$ K. Vertical white line shows the instantaneous LOL position, while the solid white line indicates the stoichiometric level curve. Black lines are level curves for $T_{amb} + 500$ K.

is detected by means of the level curve of ambient temperature plus 500 K.

However, the most important conclusion of this representation is that in all the cases small ignition kernels, appearing spontaneously due to the interaction between chemistry and flow dynamics, are detected upstream and isolated from the base of the flame. For better visualization, such hot pockets are surrounded by a white rectangle. These pockets increase in size and, finally, merge with the main flame. As Figure 16 shows, this behaviour is observed at all the boundary conditions.

This result is in line with the literature in both experimental^{31,32} and modelling^{58,61–63} fields and suggests that auto-ignition plays an important role in flame stabilization, highlighting the fundamental importance of chemistry in governing the flame structure. Considering the position of the stoichiometric contour, such ignition kernels are observed to appear both on the lean and rich sides. This result agrees with DNS simulations in the study by Tagliante et al.⁵⁸ which indicate that auto-ignition kernels occur in terms of isolated auto-ignition or assisted auto-ignition, the former being related, respectively, to rich and lean locations, the latter one assisted by the entrainment of burnt gases upstream the reaction front.

Moreover, it can occur that the lobes of the partially premixed combustion region get close enough each other to enclose fresh mixture inside the flame as observed for $t = 4$ ms in the case of $X_{O_2} = 0.21$. Again for better visualization the fresh mixture is surrounded by a rectangle.

Although difficult to quantify, in the case of $X_{O_2} = 0.13$ the base of the flame seems to be more fragmented since many isolated hot pockets are observed compared to the case of high oxygen concentration where the flame tends to be more connected. This behaviour may be caused by the faster chemistry observed for $X_{O_2} = 0.21$, which implies that chemistry tends to occur in a narrow region of the flow. This was observed in Figure 3 in Z space where it was seen that when the most reactive mixture reached the steady solution only a narrow interval of mixture fractions had reached high temperatures for this case of high oxygen concentration.

In contrast with this, in the $X_{O_2} = 0.13$ case mixtures advance in a more synchronized way, spreading the interval of mixture fractions that have reached intermediate temperatures over a wider region since chemistry is slower. This shows that the ignitable mixtures in the turbulent spray are more similar in terms of their ignition characteristics for low reactive cases than the high ones. As a consequence, ignitable spots can be found in more heterogeneous flow conditions when reactivity is low leading to a more disintegrated flame at its base. In addition, when reactivity is decreased, TCI becomes more important and completely essential to reproduce low reactivity mixtures.⁵⁷

Conclusion

The present investigation has thoroughly analysed spray A flame structure for different boundary conditions by means of LES simulations using a flamelet-based combustion model.

The flamelet profiles show that ignition is more concentrated when the oxygen content is increased, while it spreads over larger intervals of mixtures for low X_{O_2} cases. This implies more similar characteristics in terms of ignition for wider ranges of mixtures and makes possible the apparition of ignition spots in more heterogeneous conditions in the turbulent flow.

Regarding the spray, a first validation has shown that the inert spray is properly reproduced with the current configuration, showing an excellent matching with penetrations and profiles on the axis for velocity and mixing variables. Then, the investigation has followed with the description of some of the flame metrics showing that the model is able to reproduce the main flame parameters. Although in all the cases LOL predictions were underestimated, the curves were parallel to the experimental ones showing that the dependence on the boundary conditions is well-reproduced.

The instantaneous fields of the reacting fields have led to the analysis of the flame where a partially premixed combustion region is observed at the height of LOL. Such region, whose morphology is dependent on the boundary conditions, shows an extremely intense chemical activity which defines a thin layer that separates fresh from partially burnt gases and is balanced with flow dynamics producing small fluctuations of LOL. A diffusion flame that wraps the spray and is positioned downstream of this region completes the chemical reactions.

In general, negligible amounts of formaldehyde are found upstream of LOL, while acetylene is positioned downstream of the former species close to equilibrium conditions and hydroxide surrounds the stoichiometric mixture. Although the increase in reactivity leads to the augmentation of species peak values, this does not necessarily entail an increase in total mass since the acetylene total mass decreases with the oxygen concentration.

Regarding the flame stabilization mechanism, it has been shown that extinction phenomena is marginal in the development of the flame, while auto-ignition is important as the spontaneous apparition of isolated and detached ignition spots shows.

Moreover, the base of the flame tends to be more fragmented when the oxygen concentration is decreased, which is attributed to the wider ranges where flamelet ignition spreads for low-oxygen content cases.

In summary, it can be concluded that flamelet-based combustion models, in this case implemented according to the ADF model, in conjunction with LES simulations are able to reproduce the flame structure of the diesel reacting spray and, as a consequence, are suitable for their application to this complex problem.

Acknowledgements

The authors thankfully acknowledge the computational resources made available by the Red Española de Supercomputación at MareNostrum and the technical support provided by Barcelona Supercomputing Center (RES-FI-2018-1-0041).


Declaration of conflicting interests


The author(s) declared no potential conflicts of interest with respect to the research, authorship and/or publication of this article.

Funding

The author(s) disclosed receipt of the following financial support for the research, authorship and/or publication of this article: The authors acknowledge that this work was possible thanks to the Ayuda para la Formación de Profesorado Universitario (FPU 14/03278) funded by the Subprogramas de Formación y de Movilidad del Ministerio de Educación, Cultura y Deporte from Spain. Also, this study was partially funded by the Ministerio de Economía y Competitividad from Spain in the frame of the CHEST (TRA2017-89139-C2-1-R) national project.

ORCID iDs

Jose M Garcia-Oliver  <https://orcid.org/0000-0002-2676-9681>

Ricardo Novella  <https://orcid.org/0000-0002-5123-6924>

References

1. Poinot T and Veynante D. *Theoretical and numerical combustion*. Upper Marlboro, MD: RT Edwards Inc., 2005.
2. Pickett LM, Bruneaux G and Payri R. *Engine combustion network*. Livermore, CA: Sandia National Laboratories, <https://ecn.sandia.gov/>
3. Maes N, Meijer M, Dam N, Somers B, Toda HB, Bruneaux G, et al. Characterization of spray A flame structure for parametric variations in ECN constant-volume vessels using chemiluminescence and laser-induced fluorescence. *Combust Flame* 2016; 174: 138–151.
4. Bardi M, Payri R, Malbec LM, Bruneaux G, Pickett LM, Manin J, et al. Engine combustion network: comparison of spray development, vaporization, and combustion in different combustion vessels. *Atomizat Sprays* 2012; 22(10): 807–842.
5. Benajes J, Payri R, Bardi M and Martí-Aldaraví P. Experimental characterization of diesel ignition and lift-off length using a single-hole ECN injector. *Appl Therm Eng* 2013; 58(1): 554–563.
6. Payri R, Garcia-Oliver JM, Xuan T and Bardi M. A study on diesel spray tip penetration and radial expansion under reacting conditions. *Appl Therm Eng* 2015; 90: 619–629.
7. Naud B, Novella R, Pastor JM and Winklinger JF. RANS modelling of a lifted H₂/N₂ flame using an unsteady flamelet progress variable approach with presumed PDF. *Combust Flame* 2015; 162(4): 893–906.
8. Pei Y, Hawkes ER, Kook S, Goldin GM and Lu T. Modelling n-dodecane spray and combustion with the transported probability density function method. *Combust Flame* 2015; 162(5): 2006–2019.
9. Desantes JM, García-Oliver JM, Novella R and Pérez-Sánchez EJ. Application of an unsteady flamelet model in a RANS framework for spray A simulation. *Appl Therm Eng* 2017; 117: 50–64.
10. Kolmogorov AN. The local structure of turbulence in incompressible viscous fluid for very large Reynolds numbers. *Dokl Akad Nauk SSSR* 1941; 30(4): 299–303.
11. Pomraning E and Rutland CJ. A dynamic one-equation nonviscosity large-eddy simulation model. *AIAA J* 2002; 40(4): 689–701.
12. Bharadwaj N, Rutland CJ and Chang SM. Large eddy simulation modelling of spray-induced turbulence effects. *Int J Engine Res* 2009; 10(2): 97–119.
13. Mompó LJM. *Engineering large eddy simulation of diesel sprays*. PhD Thesis, Universitat Politècnica de València, Valencia, 2014.
14. Tsang CW, Kuo CW, Trujillo M and Rutland C. Evaluation and validation of large-eddy simulation sub-grid spray dispersion models using high-fidelity volume-of-fluid simulation data and engine combustion network experimental data. *Int J Engine Res*. Epub ahead of print 13 May 2018. DOI: 10.1177/1468087418772219.
15. Pope SB. Ten questions concerning the large-eddy simulation of turbulent flows. *N J Phys* 2004; 6(1): 35.
16. Pitsch H. Large-eddy simulation of turbulent combustion. *Annu Rev Fluid Mech* 2006; 38: 453–482.
17. Maas U and Pope SB. Simplifying chemical kinetics: intrinsic low-dimensional manifolds in composition space. *Combust Flame* 1992; 88(3–4): 239–264.
18. Oijen JA and Goey LPH. Modelling of premixed laminar flames using flamelet-generated manifolds. *Combust Sci Technol* 2000; 161(1): 113–137.
19. Gicquel O, Darabiha N and Thévenin D. Laminar premixed hydrogen/air counterflow flame simulations using flame prolongation of ILDM with differential diffusion. *Proc Combust Inst* 2000; 28(2): 1901–1908.
20. Pierce CD and Moin P. Progress-variable approach for large-eddy simulation of non-premixed turbulent combustion. *J Fluid Mech* 2004; 504: 73–97.
21. Ihme M and Pitsch H. Prediction of extinction and reignition in nonpremixed turbulent flames using a Flamelet/progress variable model: 1: a priori study and presumed PDF closure. *Combust Flame* 2008; 155(1–2): 70–89.
22. Ihme M and Pitsch H. Prediction of extinction and reignition in nonpremixed turbulent flames using a Flamelet/progress variable model: 2: application in LES of Sandia flames D and E. *Combust Flame* 2008; 155(1–2): 90–107.
23. Tillou J, Michel JB, Angelberger C and Bekdemir C. Large-eddy simulation of diesel spray combustion with exhaust gas recirculation. *Oil Gas Sci Technol* 2014; 69(1): 155–165.
24. Michel JB, Colin O and Veynante D. Modeling ignition and chemical structure of partially premixed turbulent flames using tabulated chemistry. *Combust Flame* 2008; 152(1): 80–99.
25. Tillou J, Michel JB, Angelberger C and Veynante D. Assessing LES models based on tabulated chemistry for the simulation of diesel spray combustion. *Combust Flame* 2014; 161(2): 525–540.

26. Michel JB and Colin O. A tabulated diffusion flame model applied to diesel engine simulations. *Int J Engine Res* 2014; 15(3): 346–369.
27. Aubagnac-Karkar D, Michel JB, Colin O and Darabiha N. Combustion and soot modelling of a high-pressure and high-temperature dodecane spray. *Int J Engine Res* 2018; 19(4): 434–448.
28. Dec JE. A conceptual model of di diesel combustion based on laser-sheet imaging. SAE technical paper 970873, 1997.
29. Wehrfritz A, Kaario O, Vuorinen V and Somers B. Large eddy simulation of n-dodecane spray flames using Flamelet generated manifolds. *Combust Flame* 2016; 167: 113–131.
30. García-Oliver JM, Malbec LM, Toda HB and Bruneaux G. A study on the interaction between local flow and flame structure for mixing-controlled diesel sprays. *Combust Flame* 2017; 179: 157–171.
31. Pickett LM, Siebers DL and Idicheria CA. Relationship between ignition processes and the lift-off length of diesel fuel jets. SAE technical paper 2005-01-3843, 2005.
32. Tagliante F, Malbec LM, Bruneaux G, Pickett LM and Angelberger C. Experimental study of the stabilization mechanism of a lifted diesel-type flame using combined optical diagnostics and laser-induced plasma ignition. *Combust Flame* 2018; 197: 215–226.
33. Pandurangi SS, Bolla M, Wright YM, Boulouchos K, Skeen SA, Manin J and Pickett LM. Onset and progression of soot in high-pressure n-dodecane sprays under diesel engine conditions. *International Journal of Engine Research* 2017; 18(5–6): 436–452.
34. Pastor JV, García-Oliver JM, Pastor JM and Vera-Tudela W. One-dimensional diesel spray modeling of multicomponent fuels. *Atomizat Sprays* 2015; 25(6): 485–517.
35. Desantes JM, García-Oliver JM, Novella R and Pérez-Sánchez EJ. Application of a flamelet-based CFD combustion model to the LES simulation of a diesel-like reacting spray. In: *Proceedings of the 10th international conference on computational fluid dynamics*, Barcelona, 9–13 June 2018. Oxford: University of Oxford.
36. Kastengren AL, Tilocco FZ, Powell CF, Manin J, Pickett LM, Payri R and Bazyn T. Engine combustion network (ECN): measurements of nozzle geometry and hydraulic behavior. *Atomizat Sprays* 2012; 22(12): 1011–1052.
37. Narayanaswamy K, Pepiot P and Pitsch H. A chemical mechanism for low to high temperature oxidation of n-dodecane as a component of transportation fuel surrogates. *Combust Flame* 2014; 161(4): 866–884.
38. Frassoldati A, D’Errico G, Lucchini T, Stagnia A, Cuocia A, Faravelli T, et al. Reduced kinetic mechanisms of diesel fuel surrogate for engine CFD simulations. *Combust Flame* 2015; 162(10): 3991–4007.
39. Akkurt B, Akargun HY, Somers LMT, Deen NG, Novella R and Pérez-Sánchez EJ. An insight on the spray-A combustion characteristics by means of RANS and LES simulations using Flamelet-based combustion models. SAE technical paper 2017-01-0577, 2017.
40. Open FOAM, 2019, <http://www.openfoam.com>
41. Senecal PK, Pomraning E, Richards KJ and Som S. An investigation of grid convergence for spray simulations using an LES turbulence model. SAE technical paper 2013-01-1083, 2013.
42. Xue Q, Som S, Senecal PK and Pomraning E. A study of grid resolution and SGS models for LES under non-reacting spray conditions. In: *Proceedings of the 25th annual conference on liquid atomization and spray systems*, Pittsburgh, PA, http://www.ilass.org/2/conferencepapers/65_2013.pdf
43. Bharadwaj N and Rutland CJ. A large-eddy simulation study of sub-grid two-phase interaction in particle-laden flows and diesel engine sprays. *Atomizat Sprays* 2010; 20(8): 637–695.
44. Beale JC and Reitz RD. Modeling spray atomization with the Kelvin-Helmholtz/Rayleigh-Taylor hybrid model. *Atomizat Sprays* 1999; 9(6): 623–650.
45. Pérez Sánchez EJ. *Application of a Flamelet-based combustion model to diesel-like reacting sprays*. PhD Thesis, Universitat Politècnica de València, València, 2019.
46. Peters N. Laminar diffusion flamelet models in non-premixed turbulent combustion. *Prog Energy Combust Sci* 1984; 10(3): 319–339.
47. Peters N. *Turbulent combustion*. Cambridge: Cambridge University Press, 2000.
48. Fiorina B, Gicquel O, Vervisch L, Carpentier S and Darabiha N. Approximating the chemical structure of partially premixed and diffusion counterflow flames using FPI flamelet tabulation. *Combust Flame* 2005; 140(3): 147–160.
49. Payri F, Novella R, Pastor JM and Pérez-Sánchez EJ. Evaluation of the approximated diffusion flamelet concept using fuels with different chemical complexity. *Appl Math Model* 2017; 49: 354–374.
50. Pera C, Colin O and Jay S. Development of a FPI detailed chemistry tabulation methodology for internal combustion engines. *Oil Gas Sci Technol* 2009; 64(3): 243–258.
51. Mastorakos E. Ignition of turbulent non-premixed flames. *Prog Energy Combust Sci* 2009; 35(1): 57–97.
52. Pickett LM, Manin J, Genzale CL, Siebers DL, Musculus MPB and Idicheria CA. Relationship between diesel fuel spray vapor penetration/dispersion and local fuel mixture fraction. *SAE Int J Engines* 2011; 4: 764–799.
53. Meijer M, Malbec LM, Bruneaux G and Somers LMT. Engine combustion network: spray A basic measurements and advanced diagnostics. In: *Proceedings of the 12th triennial international conference on liquid atomization and spray systems (ICLASS 2012)*, Heidelberg, 2–6 September 2012. Eindhoven: Eindhoven University of Technology.
54. Eagle WE, Musculus MPB, Malbec LMC and Bruneaux G. Measuring transient entrainment rates of a confined vaporizing diesel jet. In: *Proceedings of the Americas 26th annual conference on liquid atomization and spray systems*, Portland, OR, <https://www.osti.gov/servlets/purl/1141483>
55. Olbricht C, Ketelheun A, Hahn F and Janicka J. Assessing the predictive capabilities of combustion LES as applied to the Sydney flame series. *Flow Turbul Combust* 2010; 85(3–4): 513–547.
56. Novella R, García A, Pastor JM and Domenech V. The role of detailed chemical kinetics on CFD diesel spray ignition and combustion modelling. *Math Comput Model* 2011; 54(7): 1706–1719.

57. Bhattacharjee S and Haworth DC. Simulations of transient n-heptane and n-dodecane spray flames under engine-relevant conditions using a transported pdf method. *Combust Flame* 2013; 160(10): 2083–2102.
58. Tagliante F, Poinso T, Pickett LM, Pepiot P, Malbec LM, Bruneaux G and Angelberger C. A conceptual model of the flame stabilization mechanisms for a lifted diesel-type flame based on direct numerical simulation and experiments. *Combust Flame* 2019; 201: 65–77.
59. Duwig C and Fuchs L. Large eddy simulation of a H₂/N₂ lifted flame in a vitiated co-flow. *Combust Sci Technol* 2008; 180(3): 453–480.
60. Venugopal R and Abraham J. A review of fundamental studies relevant to flame lift-off in diesel jets. SAE technical paper 2007-01-0134, 2007.
61. Gong C, Jangi M and Bai XS. Large eddy simulation of n-dodecane spray combustion in a high pressure combustion vessel. *Appl Energy* 2014; 136: 373–381.
62. Pei Y, Som S, Pomraning E, Senecal PK, Skeen SK, Manin J and Pickett LM. Large eddy simulation of a reacting spray flame with multiple realizations under compression ignition engine conditions. *Combust Flame* 2015; 162(12): 4442–4455.
63. Kahila H, Wehrfritz A, Kaario O, Masouleh MG, Maes N, Somers B and Vuorinen V. Large-eddy simulation on the influence of injection pressure in reacting spray A. *Combustion and Flame* 2018; 191: 142–159.